

Structure and Stoichiometry in Supervalent Doped $\text{Li}_7\text{La}_3\text{Zr}_2\text{O}_{12}$

Saikat Mukhopadhyay,[†] Travis Thompson,[‡] Jeff Sakamoto,[‡] Ashfia Huq,[§] Jeff Wolfenstine,^{||} Jan L. Allen,^{||} Noam Bernstein,[⊥] Derek A. Stewart,[†] and M. D. Johannes^{*,⊥}

[†]Cornell Nanoscale Facility, Cornell University, Ithaca, New York 14853, United States

[‡]Department of Chemical Engineering and Materials Science, Michigan State University, East Lansing, Michigan 48824, United States

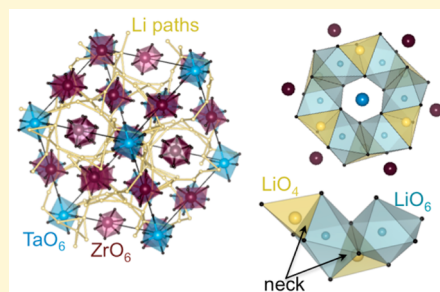
[§]Oak Ridge National Laboratory, Oak Ridge, Tennessee 37830, United States

^{||}Army Research Laboratory, Adelphi, Maryland 20783, United States

[⊥]Center for Computational Materials Science, Naval Research Laboratory, 4555 Overlook Avenue SW, Washington, DC 20375, United States

S Supporting Information

ABSTRACT: The oxide garnet material $\text{Li}_7\text{La}_3\text{Zr}_2\text{O}_{12}$ shows remarkably high ionic conductivity when doped with supervalent ions that are charge compensated by Li vacancies and is currently one of the best candidates for development of a technologically relevant solid electrolyte. Determination of optimal dopant concentration, however, has remained a persistent problem due to the extreme difficulty of establishing the actual (as compared to nominal) stoichiometry of intentionally doped materials and by the fact that it is still not entirely clear what level of lattice expansion/contraction best promotes ionic diffusion. By combining careful synthesis, neutron diffraction, high-resolution X-ray diffraction (XRD), Raman measurements, and density functional theory calculations, we show that structure and stoichiometry are intimately related such that the former can in many cases be used as a gauge of the latter. We show that different Li-vacancy creating supervalent ions (Al^{3+} vs Ta^{5+}) affect the structure very differently, both in terms of the lattice constant, which is easily measurable, and in terms of the local structure, which can be difficult or impossible to access experimentally but may have important ramifications for conduction. We carefully correlate the lattice constant to dopant type/concentration via Vegard's law and then further correlate these quantities to relevant local structural parameters. Our work opens the possibility of developing a codopant scheme that optimizes the Li vacancy concentration and the lattice size simultaneously.



I. INTRODUCTION

All-solid-state Li ion batteries are highly desirable to avoid the well-known problems of dendrite-driven short circuit and/or thermal runaway^{1,2} that plague liquid electrolyte cells, but development of such a battery has been limited by the extremely low ionic conductivity of most candidate solid Li^+ electrolyte compounds. A typical liquid electrolyte exhibits an ionic conductivity of $\sigma \sim 10^{-2}$ S/cm, whereas typical solid electrolytes are a full 4 orders of magnitude less conductive with $\sigma \sim 10^{-6}$ S/cm.³ The recent discovery of garnet structured oxide, $\text{Li}_7\text{La}_3\text{Zr}_2\text{O}_{12}$, with $\sigma \sim 10^{-4}$ S/cm, chemical stability against both Li metal (anode) and LiCoO_2 (cathode),⁴ along with a suitable electronic band gap⁵ has therefore been considered a possible breakthrough in finally achieving this technology.

$\text{Li}_7\text{La}_3\text{Zr}_2\text{O}_{12}$ (LLZO) was originally identified as a fast Li^+ conductor by Murugan et al.,⁶ but progress to develop it was hampered by the fact that synthesis sometimes resulted in a tetragonal phase with a significantly lower conductivity, rather than the desired high conductivity cubic phase.⁷ The determining factor in the phase formation was finally resolved when it was noticed that LLZO synthesized in Al-containing

(Al_2O_3) crucibles sometimes crystallizes as the cubic polymorph and sometimes as the tetragonal polymorph, whereas synthesis in Pt-only crucible yielded purely the tetragonal phase.⁸ Subsequent experiments with intentional doping⁹ confirmed that incorporation of Al plays a key role in achieving the high conductivity cubic phase. Computational results¹⁰ revealed that the underlying mechanism was 2-fold: supervalent Al^{3+} on the Li sublattice was charge balanced by the creation of two Li^+ vacancies. With enough of these vacancies, the ordering of the Li sublattice was destroyed, and the resultant disorder, in combination with a lattice relaxation, produced the cubic phase. These same vacancies are also responsible for opening up previously blocked Li^+ hopping paths leading to an enhanced conductivity.

Importantly, it has been shown that Al is not uniquely required to achieve the cubic phase. Other supervalent dopants, such as Nb, Ga, and Ta, can also create the necessary Li vacancies and thereby produce a cubic lattice with increased

Received: January 28, 2015

Revised: April 17, 2015

Published: April 20, 2015

conductivity.⁹ Since Al preferentially sits on the Li sublattice and partially blocks the ionic diffusion routes, choosing an alternate dopant that locates away from the diffusion paths is likely to be the best route to achieving the highest ionic conductivity.⁹ Although the minimum vacancy concentration for transition to the high conductivity phase is known,^{10,11} there is as of yet no agreed upon value for optimal dopant type or concentration. Additionally, dopants change the overall lattice size and shape as well as the width of ionic conduction channels. Whether it is stoichiometry or geometry that primarily determines the maximal conductivity of LLZO is therefore undetermined, and attempts to push it even higher are ongoing. The major barriers toward establishment of an optimal system are that (a) the nominal and actual concentrations of dopant ions may differ, (b) the equivalency between number of dopants (even when perfectly established) and number of Li vacancies can be altered by the presence of other common defects, particularly oxygen vacancies, and (c) the effect of lattice size and especially Li^+ channel size on ionic mobility is unknown. Thus, each component of the system must be known precisely, and further, the effect of each component on the lattice must be known.

In this work, we bring together the results of a variety of experimental techniques along with calculations based on first-principles density functional theory (DFT) to provide a straightforward analysis of the stoichiometry and resulting structure of a carefully synthesized series of doped LLZO samples, nominally $\text{Li}_{7-x}\text{La}_3\text{Zr}_{2-x}\text{Ta}_x\text{O}_{12}$. We compare data from Raman spectroscopy, high resolution XRD, and neutron diffraction measurements to DFT calculations and find that the lattice couples strongly to both type and concentration of dopants/defects such that lattice effects themselves can be used to evaluate the stoichiometry. Using calculations, we identify two easily separable dopant peaks in the Raman spectra and use these to establish experimental Ta dopant concentration and compare to high resolution XRD that gives the same information. We use neutron diffraction to establish the number of Li ions present. We use DFT calculations to show how Ta dopants, Al dopants, Li vacancies, and oxygen vacancies change Vegard's law and internal structural variables. We illustrate how unintentional incorporation of oxygen vacancies or of Al (via sintering in alumina crucibles) may affect measured properties and conduction. By bringing these various experimental and computational methodologies together and making close comparisons between them, we provide a "roadmap" of the relationship between structure and stoichiometry for this class of materials. We believe this will aid in diagnosing the "true" stoichiometry of samples without the need for performing the entire suite of extensive cross-characterization that was necessary for this study. Furthermore, our clearly established and quantitative linking of the stoichiometry and structure will allow the intentional design of materials with both specific Li ion vacancy concentrations and specific lattice size, the two factors currently thought to determine overall ionic conductivity, at the same time.

II. METHODS

Theoretical Calculations. We employed the projector augmented wave (PAW)^{12,13} approach within the Generalized Gradient Approximation (GGA) of density functional theory where we used the Perdew-Burke-Ernzerhof (PBE)^{14,15} exchange-correlation functional as implemented in VASP.^{16,17} We use unit cells of four formula units for phonon calculations to reproduce the Raman spectra and unit

cells of eight formula units for lattice constant calculations. All structures were fully optimized relaxing both the lattice parameters and ions. A $4 \times 4 \times 4$ Monkhorst-Pack grid was used for k-point sampling of the Brillouin zone of the unit cell with an energy cutoff of 550 eV. The self-consistency convergence criterion for the energy was set to 10^{-5} eV, and geometry relaxation was considered converged when all forces were less than 10^{-2} eV/Å. To simulate the doped and disordered cubic cell, $\text{Li}_{7-x}\text{La}_3\text{Zr}_{2-x}\text{Ta}_x\text{O}_{12}$, we replaced a fraction of Zr atoms with Ta atoms and removed an equal number of Li atoms, and for doped and disordered $\text{Li}_{7-3x}\text{Al}_x\text{La}_3\text{Zr}_2\text{O}_{12}$, we replaced a fraction of Li atoms by Al and removed two further Li to charge compensate. Cells depleted in this manner for Ta concentrations $x = 0.25, 0.5, 1.0$, and 1.5 for all Al concentrations were subject to 100 ps of molecular dynamics simulation at 800 K with variable cell shape to achieve true disorder and then rerelaxed using standard ($T = 0$) DFT techniques. Other Ta concentrations were extrapolated by randomly removing Li from one of the previously heated and relaxed compounds and again relaxing at $T = 0$. Cells with Li and O vacancies ($2V_{\text{Li}} - V_{\text{O}}$) were simulated by using previously created Ta-doped cells and randomly removing twice as many Li as O and fully relaxing the cell and internal parameters.

The phonon density of states of the disordered cells was then obtained using the VASP-phonopy¹⁸ interface based on the zone centered (Γ -point) frequencies. A $2 \times 2 \times 2$ Monkhorst-Pack grid was used to calculate the force constants in these garnet oxides. The interatomic force constants were calculated based on the Hessian matrix using density functional perturbation theory (DFPT) in which the projection operators were evaluated in reciprocal space.

Materials. Samples of composition $\text{Li}_{7-x}\text{La}_3\text{Zr}_{2-x}\text{Ta}_x\text{O}_{12}$ ($x = 0.25, 0.5, 0.75$, and 1.50) were prepared using a coprecipitation process. Li_2CO_3 , $\text{La}(\text{OH})_3$, and $[\text{ZrO}_2]_2 \cdot \text{CO}_2 \cdot x\text{H}_2\text{O}$ (zirconium carbonate, basic hydrate; equivalent ZrO_2 content determined from thermogravimetric analysis) weighed in the desired stoichiometry were dissolved in ~ 1.4 M HNO_3 (aq). A 6 wt % excess of Li was used to compensate for Li volatilization during synthesis. The stoichiometric amount of TaCl_5 was first dissolved in anhydrous ethanol and then added to the Li, La, and Zr containing precursor solution. The resulting solution was evaporated to dryness in a microwave oven contained inside a fume hood. Evolution of NO_x was observed during this step. The dried coprecipitate was lightly ground with a mortar and pestle and pressed into a pellet using a Carver laboratory die and press. The pellet was placed on a ZrO_2 plate and heated in air at 1173 K for 3–4 h. The furnace was turned off, and the sample was removed. All samples were loaded in sealed vanadium cans inside a glovebox to prevent exposure to air.

Neutron Diffraction. Time of flight neutron powder diffraction data was collected at room temperature (300 K) and 10 K for $\text{Li}_{7-x}\text{La}_3\text{Zr}_{2-x}\text{Ta}_x\text{O}_{12}$ (where $x = 0.25, 0.5, 0.75$, and 1.5) at Powgen, the general purpose powder diffraction instrument at the Spallation Neutron Source, Oak Ridge National Laboratory. Two data sets were collected at each temperature using center wavelengths 1.066 and 2.665 Å covering a d -spacing range of 0.3–6.5 Å.

High Resolution XRD. High resolution synchrotron powder X-ray diffraction data were collected using beamline 11-BM at the Advanced Photon Source (APS), Argonne National Laboratory using an average wavelength of 0.414 Å. Discrete detectors covering an angular range from -6 to 16° 2θ are scanned over a 34° 2θ range, with data points collected every 0.001° 2θ and a scan speed of $0.01^\circ/\text{s}$. Rietveld structural refinements of both neutron and synchrotron X-ray diffraction data were performed using GSAS with EXPGUI to determine the Ta and Zr content.^{19,20}

Raman Spectroscopy. Raman spectra were collected with a Renishaw inVia Raman microscope using a 514 nm laser, 1800 lines/mm holographic grating, and 20X magnification.

III. RESULTS AND DISCUSSION

Establishing Structure and Stoichiometry. Figure 1 shows a neutron diffraction spectrum and fit for one of our doped compounds (nominal stoichiometry

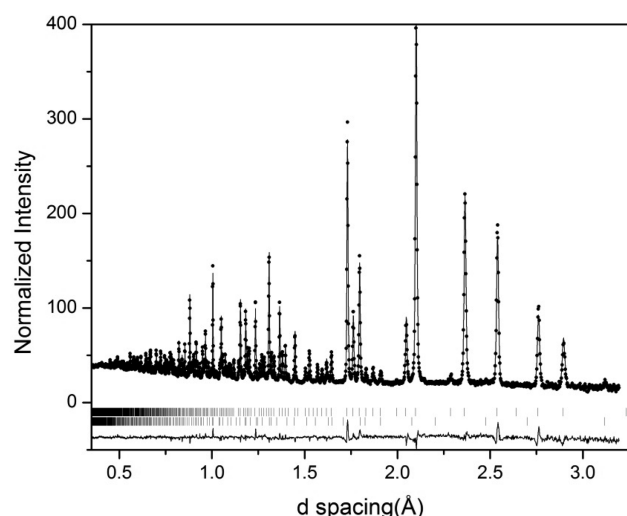


Figure 1. Neutron diffraction spectrum and the corresponding Rietveld fit ($R_{wp} = 3.5\%$) for $\text{Li}_{6.5}\text{La}_3\text{Zr}_{1.5}\text{Ta}_{0.5}\text{O}_{12}$ (nominal stoichiometry). Dots indicate collected data; lines through them are the model fit along with difference curve shown in the bottom. The series of tick marks on top belongs to the primary cubic garnet phase, and the ones on the bottom indicate the location of the pyrochlore phase $\text{La}_2\text{Zr}_2\text{O}_7$ which is present at the level of less than 2 wt %. The data extracted from these fits are given in Table 1.

$\text{Li}_{6.5}\text{La}_3\text{Zr}_{1.5}\text{Ta}_{0.5}\text{O}_{12}$). The excellent quality of the fit is representative of the entire series, and the data extracted from these fits are given in Table 1 along with refinement data from our synchrotron XRD experiments and DFT calculated lattice parameters. We took ND at 300 K for ease of comparison with other published results; however, because of the extreme mobility of the Li^+ ions, it was necessary to take another set of data at 10 K to accurately establish the Li concentration. Li positions were indexed to two separate symmetry sites: 96h (octahedral) and 24d (tetrahedral). Attempts to index to other sites decreased the goodness of fit. A full set of the 300 K spectra and parameter tables can be found in Thompson et al.²¹ and are included in the Supporting Information (T1–T3). We used synchrotron XRD to establish the Ta content, which is consistently slightly higher than the nominal value, while the Li content, as established by ND (10 K), is consistently lower than the nominal value. The two deviations from nominal stoichiometry are not offsetting, however, as the Li deficiency is greater than the surplus of Ta. The highly mobile nature of the Li^+ ions may cause some amount of the Li to be located away from the symmetry sites used to count Li occupation even at 10 K, or it is possible that extra Li vacancies do exist and are charge compensated by an alternate mechanism such as the oxygen vacancies as we suggest in this work. Due to the inability to perform ICP on anions, such as oxygen, and also because of the relatively low Li

resolution limit in LLZO ($\sim \pm 0.5$ mol), inductively coupled plasma (ICP) was not pursued to verify the Li/O stoichiometry.

Our synchrotron XRD data also indicate that for $x < 1.5$, there is some amount of phase separation such that multiple cubic phases exist together. Interestingly, including multiple cubic phases in our ND fits decreases the goodness of fit as observed previously for Al doped LLZO compositions.²⁰

We use density functional theory to calculate the lattice constants of an entire sequence of $\text{Li}_{7-x}\text{La}_3\text{Zr}_{2-x}\text{Ta}_x\text{O}_{12}$ compounds with $x = 0$ through $x = 2$ in steps of $x = 0.25$, such that all investigated compounds are included. We note that the cleanest comparison between computational and measured structural data will be for the tetragonal, ordered system. This is because the tetragonal distortion is predicated on Li ordering, which is in turn predicated on the existence of only very small deviations from Li stoichiometry.^{10,22} Therefore, observation of a tetragonal system implies very few defects, particularly with respect to Li vacancies, which are the trigger for transition to a cubic system. Our calculated lattice constants for the $x = 0$ system are $a = 13.2103$ Å and $c = 12.6756$ Å, in excellent agreement with previously measured values for LLZO with confirmed absence of Al ($a = 13.103$ Å and $c = 12.6542$ Å; $a = 13.097$ Å²³ and $c = 12.67$ Å²⁴) and with the normal slight overestimation ($\sim 1\%$), common to DFT calculations that employ the GGA exchange-correlation functional.²⁵ As we add Ta to the system, the calculated lattice parameters decrease smoothly throughout the series according to Vegard's law. For ease of comparison between various experimental values and our computational results, we shift all of our lattice constants by the amount needed to bring theory and experiment into agreement at $x = 0$ where, as previously mentioned, we believe the synthesized and modeled compounds to be most precisely matched in stoichiometry. These calculated values, both before and after the shift, are shown together with measured values from this work and from several other published reports in Figure 2.

There are two important things to note in Figure 2. The first is that our experimental volume data lines sit below those previously reported. This is likely because alumina crucibles were used in the other studies, and accidental incorporation of small amounts of Al into the structure during synthesis is certainly possible. As we will discuss quantitatively in a later section, Al incorporation expands the lattice. Thus, the uniformly larger lattice constants in uncontrolled synthesis (i.e., using alumina crucibles) compared to Al-free synthesis at the same intentional dopant level^{26–30} can be taken as a strong sign of the existence of Al impurities. Another complication comes from the fact that exposure to air changes the lattice in an uncontrolled manner,³¹ and this may affect some of the data in Figure 2. Since we have sealed our samples in vanadium cans

Table 1. Extracted Concentration and Lattice Parameter Data from the Fits of the ND, XRD, and DFT for $\text{Li}_{7-x}\text{La}_3\text{Zr}_{2-x}\text{Ta}_x\text{O}_{12}$ with Various x

	$\text{Li}_{6.5}\text{La}_3\text{Ta}_{0.5}\text{Zr}_{1.5}\text{O}_{12}$	$\text{Li}_{6.25}\text{La}_3\text{Ta}_{0.75}\text{Zr}_{1.25}\text{O}_{12}$	$\text{Li}_{5.5}\text{La}_3\text{Ta}_{1.50}\text{Zr}_{0.5}\text{O}_{12}$
Ta content (XRD 300 K refined)	0.52 ± 0.002	0.79 ± 0.002	1.56 ± 0.002
Li content (ND 10 K refined)	6.13 ± 0.182	6.01 ± 0.088	4.69 ± 0.124
a_{exp} (ND) 300 K	12.9305(1)	12.9086(1)	12.8343(1)
a_{exp} (ND) 10 K	12.9160(2)	12.8878(1)	12.8179(2)
a_{theory}	13.00	12.98	12.90

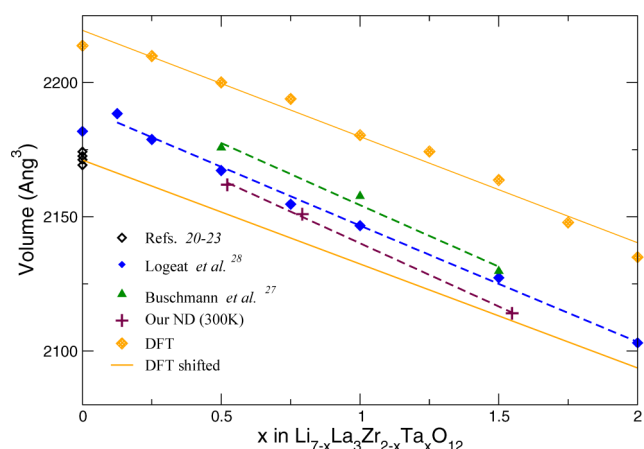


Figure 2. Variation of the lattice parameter of $\text{Li}_{7-x}\text{La}_3\text{Zr}_{2-x}\text{Ta}_x\text{O}_{12}$ as a function of dopants (x). The shifted DFT line is generated by bringing the DFT and measured values for the ordered, tetragonal cell into agreement.

inside the glovebox, we believe our measurements represent the lattice constants of materials uncontaminated by air or by Al.

These impurities significantly complicate performance analysis since Al incorporation also produces Li vacancies, which are known to affect conductivity. The second important point is that there is excellent overall agreement in the slope of the line between experiment and theory. However, somewhere below $x = 0.5$, all of the experimental data sets exhibit a violation of Vegard's law, while the computational data does not. This can be seen most clearly in the data of Logeat et al.²⁸ which spans the entire range of possible Ta doping and shows the curious dip between the $x = 0.2$ and $x = 0$ compounds. For the other data sets, one can observe the same violation by extrapolating their Vegard's slope to the y -axis and comparing the intercept to the tight cluster of measured values at $x = 0$. Other recent data for Ta-doped compounds with uncontrolled Al incorporation due to alumina crucibles³² shows a similar expansion of the lattice of between 1% and 2.5% throughout the series.

It is important to note that the kink in the experimental data is significantly larger than the calculated one, and the calculated one may simply be a fluctuation in the computational data on the order of what can be seen in many of the points that deviate from the fitted line. This is especially true for the Al-free, Ta-

doped compounds of this work. The discontinuity, then, can be taken as a signal that something about the stoichiometry, aside from the known dopant level, is changing. Previous work has shown¹¹ that $\text{Li}_{7-x}\text{La}_3\text{Zr}_{2-x}\text{Ta}_x\text{O}_{12}$ does not form a continuous series of solid solution compounds for all x , but rather that there is a critical dopant value, $x_c = 0.5$, below which the compound separates into $x = 0$ and $x = x_c$ components. Interestingly, x_c appears to coincide with the critical value for transition to a cubic system $x \approx 0.5$. Pure cubic phase compounds for $0 < x < 0.5$ do not exist, and measured values in this region likely correspond to mixed tetragonal/cubic phase materials. Thus, the discontinuities seen in Figure 2 can be attributed to the existence of mixed phases in the compounds below $x = 0.5$.

To investigate further the contraction of the lattice due to Ta and its microscopic origins, we calculate and measure the Raman spectra of $\text{Li}_{7-x}\text{La}_3\text{Zr}_{2-x}\text{Ta}_x\text{O}_{12}$ for a variety of values of x . The calculated phonon density of states (PHDOS) and the measured Raman spectra of LLZO in the tetragonal (t-LLZO) phase are shown in Figure 3(a). Our PHDOS contains both Raman and IR derived peaks so that quantitative agreement is impossible. However, the highest frequency Raman-active peak at $\sim 640 \text{ cm}^{-1}$ is Raman only and separated in energy from any IR-active peaks. This portion of the spectrum is in excellent agreement with experiment and is the subject of interest for this work. A partial PHDOS projected onto the individual atoms in Figure 3(b) reveals that the peak of interest is composed mainly of oxygen, with small contributions from Li and from (very small) Ta. By narrowing in on only the energy range of this particular phonon mode, we have determined that it is a symmetric breathing mode of the oxygen octahedron around the Zr ion. A video (V1) of this mode is provided in the SI.

Evolution of the high frequency part of the experimental Raman-spectra as a function of Ta-dopants is shown in Figure 4 along with the calculated PHDOS. As the concentration of dopant (Ta) increases, a peak near 720 cm^{-1} appears and then grows in intensity while the Zr-associated peak decreases. A visual inspection of the phonons associated with the 720 cm^{-1} peak confirms that it is a breathing mode of oxygen against Ta, analogous to the Zr–O breathing mode previously described. That the breathing mode around Ta has a higher frequency than the same mode around Zr indicates that the Ta–O bond is shorter than the Zr–O bond, which is also confirmed by the results of our DFT calculations. This contraction around the

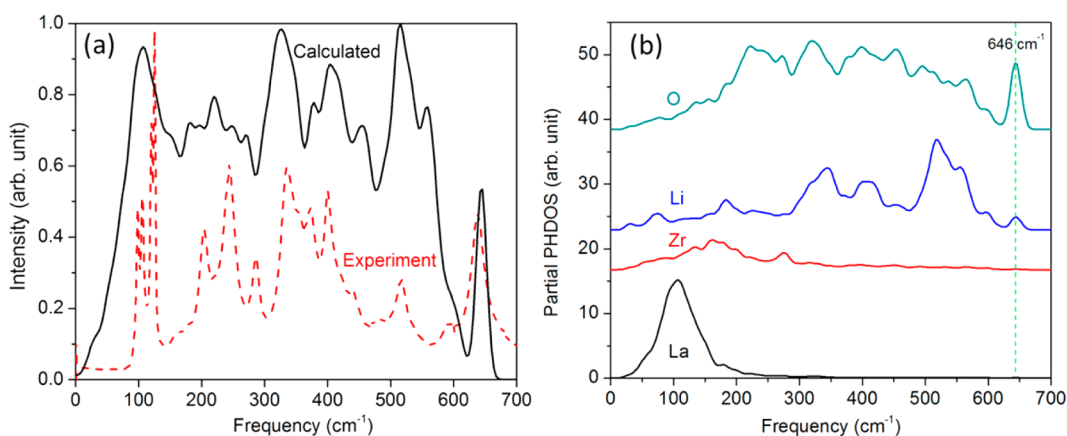


Figure 3. (a) Calculated phonon density of states (black line) and measured Raman intensity (red dashed line) for LLZO in the tetragonal phase. (b) Partial phonon density of states of LLZO projected on La, Zr, Li, and oxygen atoms.

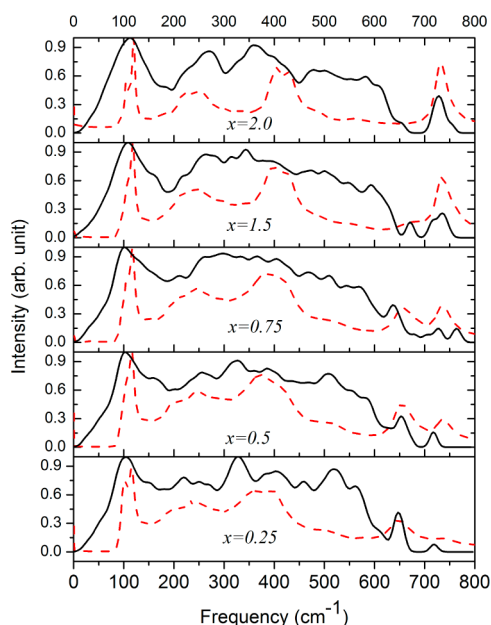


Figure 4. Calculated phonon density of states (black solid lines) and measured Raman intensity LLZO (red dashed lines) for $\text{Li}_{7-x}\text{La}_3\text{Zr}_{2-x}\text{Ta}_x\text{O}_{12}$ as a function of x .

dopant ion is the main source of the reduction in volume that gives rise to the negative slope of the Vegard's law line in Figure 2. The Raman spectrum (and PHDOS) of cubic LLZO is notably smoother compared to the case of t-LLZO due to enhanced disorder (reduced symmetry, see Figure S1 in the Supporting Information) in the cubic phase similar to the case with Al-doped LLZO.²⁶ There is continued good agreement between experiment and theory, though a splitting in the theoretical peaks appears, most notably $x = 0.75$. Such splittings can be attributed to accidental long-range ordering of Li ions due to the "small" (4 formula units) supercell used in the calculations, necessary for reasonable computational time. By manipulating the distribution of Ta/Zr and Li vacancies, these splittings can be changed (see Figure S2 in the Supporting Information), thereby confirming their relationship to order/disorder, but a truly long-range disorder that would eliminate them entirely remains computationally out of reach. In most experimental cases, we believe the Li sublattice to be fully disordered, but a similar splitting observed in Raman-spectra of Sb-doped³³ LLZO may be attributable to unintentional ordering.

We have extracted the relative normalized weight of the characteristic peaks from the ZrO_6 and TaO_6 breathing modes in the Raman spectra by directly integrating the area in the calculated PHDOS and by fitting each peak to a Gaussian and then integrating in the experimental spectra (this is to eliminate the frequency-dependent background). In the results plotted in Figure 5, it is important to note that the x -axis is the *nominal* Ta concentration for the experimental points (nominal and actual are identical for the computational points). At both end points, where disorder is at a minimum, the experimental and theoretical points align perfectly, while in the mid-region the experimental Raman intensities deviate from perfect linearity with the end points and indicate a *slight* surplus (deficit) of Ta (Zr) compared to the nominal values in excellent agreement with our findings from high resolution XRD data. Note also the clear jump in the experimental data in going from the undoped,

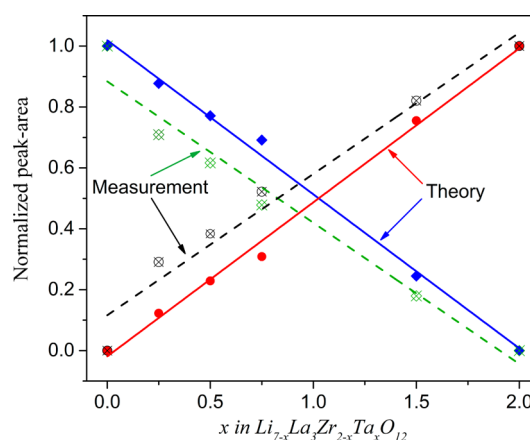
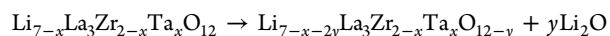


Figure 5. Normalized peak area (weight) of Zr- and Ta-peak of $\text{Li}_{7-x}\text{La}_3\text{Zr}_{2-x}\text{Ta}_x\text{O}_{12}$ as a function of x . Normalized peak area = $A_{\text{Zr(Ta)}} \times 1/(A_{\text{Zr}} + A_{\text{Ta}})$ where $A_{\text{Zr(Ta)}}$ is the individual peak-area due to Zr(Ta) breathing mode. The dashed (solid) lines are the linear fit to the experimental (theoretical) data. Red/black lines correspond to Ta peak weight, and blue/green lines correspond to Zr peak weight.

Ta = 0, tetragonal LLZO to the doped, cubic compounds that echoes the jump seen in the measured lattice constants of Figure 2. Once again, there is no similar discontinuity in the computational data.

Now we turn to the issue of the excess Li vacancies revealed by ND in our carefully synthesized Al-free compounds, and the possible issue of unintentional Al incorporation (and the associated Li vacancies) in previous uncontrolled synthesis reports. In the latter case, it is well-known that each Al^{3+} ion enters the lattice at a Li site, expelling 3 Li^+ ions and thereby creating two Li vacancies. However, for the Al-free compounds where excess Ta has been eliminated as a significant contributor to the Li deficiency, we must seek an alternative mechanism for charge compensation. One obvious culprit is oxygen vacancies, which occur commonly in other wide band gap oxides.^{34–39} Each oxygen vacancy would require two Li vacancies for charge balance, written in Kroger-Vink notation as $\emptyset = 2V_{\text{Li}}' + V_{\text{O}}^{\bullet\bullet}$. We note that all measured lattice constants are slightly to somewhat higher than the shifted DFT calculated ones, with the exception of $x = 0$ where they have been forced to match. We calculate the cell volume for oxygen vacancies compensated by Li vacancies for each concentration of Ta as well as for Al dopant incorporation compensated by Li vacancies. Figure 6 shows the results of these calculations (a limited selection of the oxygen vacancy results has been chosen for clarity). Al contamination and oxygen vacancy formation both expand the lattice, each producing its own Vegard's law, and both of which differ in both magnitude and direction from the Vegard's law established by Ta doping. This provides not only a possible explanation for the difference between theory and experiment but also a possibility to quantify the number of actual Li vacancies based on the lattice discrepancy. The likelihood of accidental oxygen vacancy defects can be estimated by calculating the formation energy of such defects. We do so by calculating the energy of the following reaction



for a variety of x (Ta concentrations) and y (defect complex concentrations). The reaction energy increases approximately linearly from 0.8 eV at $x = 0.25$ to 3.0 eV at $x = 1.75$. This indicates that the defect pair, $2V_{\text{Li}}' + V_{\text{O}}^{\bullet\bullet}$, is significantly more

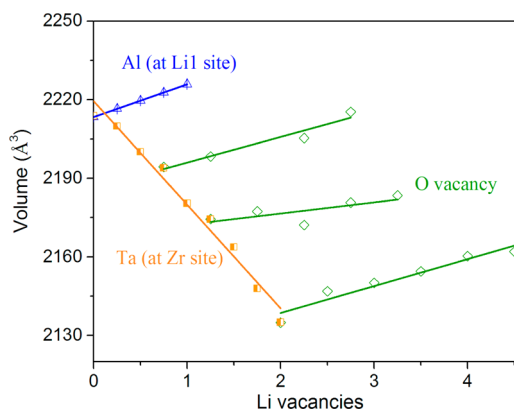


Figure 6. Variation of lattice parameter of Ta dopants, Al dopants, and O vacancies. Each quantity is plotted in terms of the number of Li site vacancies it creates per formula unit of undoped LLZO. O vacancy calculations were performed at each Ta concentration, but only three representative data sets are included in the plot, namely $\text{Li}_{6.25-2y}\text{La}_3\text{Zr}_{1.25}\text{Ta}_{0.75}\text{O}_{2-y}$, $\text{Li}_{5.75-2y}\text{La}_3\text{Zr}_{0.75}\text{Ta}_{1.25}\text{O}_{2-y}$, and $\text{Li}_{5.0-2y}\text{La}_3\text{Ta}_{2.0}\text{O}_{2-y}$ where in this notation y corresponds to the number of oxygen vacancies or twice the number of Li vacancies as plotted along the x axis. To recover the number of dopants per formula unit, the following conversions apply: 1 Ta = 1 Li vacancy, 1 Al = 2 Li vacancies, 1 O vacancy = 2 Li vacancies.

likely to form at low Ta doping levels than at high ones. This is in good correspondence with the discrepancy between our calculations and experimental measurements of the lattice constant, which is greater at low Ta doping levels and shrinks to nearly zero at high Ta doping levels. It is interesting to note that control of Li vacancy concentration via oxygen vacancy creation has been suggested⁴⁰ and that the existence of oxygen vacancies as an accidental inclusion has also been postulated.⁴¹ A particularly interesting case is that of Xie et al.⁴² in which an Al-free cubic LLZO was synthesized. Without any intentional dopants to charge compensate the Li vacancies, one could surmise that oxygen vacancies filled the role. The significantly larger than usual observed lattice constant in that system is perfectly consistent with our hypothesis that the existence of oxygen defects that compensate the Li vacancies serve to expand the structure.

The slope varies from $0.030 \text{ Å/V}_\text{O}$ to $0.092 \text{ Å/V}_\text{O}$ with the two maximal points stemming from the (artificial) limits of creating oxygen vacancies bonded only to Zr or only to Ta. Most of the values have significantly less spread and fall within $0.012 \text{ Å/V}_\text{O}$ of the average value, $0.048 \text{ Å/V}_\text{O}$. Assuming the vacancies are created randomly at the high temperatures generally used for synthesis, the average value should best represent physical conditions.

We have plotted the Vegard's law as a function of the Li vacancies created by each dopant in Figure 6, but since an oxygen vacancy produces two Li vacancies, a Ta dopant produces only one, and an Al dopant produces three (but then occupies one of them), it may in some cases be more useful to know the volume as a function of dopant number instead. For this purpose, a full table of the various Vegard's laws as a function of dopant concentration or vacancy concentration is in the Supporting Information (T4).

Ramifications for Ionic Conductivity. It is well agreed upon that the Li vacancy concentration is a crucial factor in the ionic conductivity of LLZO and that optimization of this concentration is essential for extracting the highest possible

performance. Indeed one of the main motivations of this work was to formulate a method by which the vacancy concentration could be accurately established. However, it is certainly not the *only* factor that contributes. Since Li ions must hop from site to site, the activation barrier between sites also plays a large role. In Figure 7 we show a portion of the Li^+ ion pathway and a

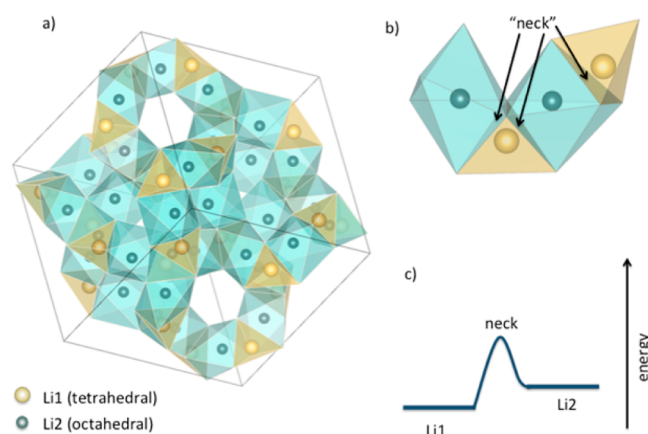


Figure 7. a) The cubic LLZO lattice with only the tetrahedral Li1 sites and octahedral Li2 sites shown. The oxygens that define the two sites are eliminated for clarity along with the other elements (La, Zr, Ta, Al, etc...). b) A section of the Li ion pathway showing the Li1–Li2–Li1–Li2 hopping path that carries ions through the material. Each transition from site to site occurs through the indicated triangular “neck”. c) A schematic of energy dependencies from typical transition state theory.

schematic of the relevant energies involved in hopping. There are two stable sites: a tetrahedrally coordinated one (Li1) and an octahedrally coordinated one (Li2). To travel between sites, the Li^+ ion must pass through a triangular “neck”. The stability of the ion at each site and the energy barrier as it passes through the neck combine to determine the activation potential, which enters the conductivity as $e^{(-E_a/kT)}$. The size of the octahedron/tetrahedron and neck will therefore all have an effect on the conductivity by shifting the site energies and/or neck energy. Some researchers have suggested that one can correlate the size of the lattice to the conductivity,⁴³ but this is simply a proxy for the three aforementioned factors that together are known as the channel size or channel width. It is not yet known whether a larger or smaller channel width is more beneficial for transport, since there might be a trade-off between increased/decreased site stability and a corresponding decrease/increase in the energy barrier at the neck. Previous computational work suggests that a simple uniform expansion or contraction that acts equally on site size and neck size does little to change the overall conductivity⁴⁴ which, in combination with observed large changes in conductivity, may indicate that separate control of the two structural aspects is important for manipulating Li ion diffusion. A detailed theoretical study of the energetics of the initial and final states and the hopping barrier as a function of changing each aspect of the microscopic structure is therefore much desired but is beyond the scope of this work. We can, however, provide information about how the channel width changes as a function of dopants and/or impurities that, in combination with future knowledge of the relationship between the expansion/contraction of the relevant structural components and the shift in the energy barrier, will provide a map for the optimal structure. In Figure 8, we show

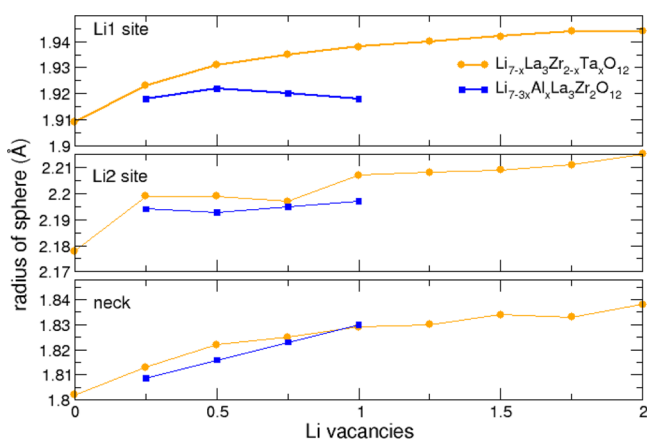


Figure 8. Radius of the sphere that (top panel) fits within the four nearest neighbors of the tetrahedral Li1 site, (second panel) fits within the octahedral Li2 site, and (third panel) subtends the neck connecting Li1 and Li2 sites.

how the two Li site sizes and the triangular window between them change with doping. The site sizes are evaluated by placing an expandable sphere (balloon) at each Li site throughout the lattice and allowing it to both expand and drift until its perimeter is in contact with four oxygen atoms. We record as the site size the radius of the balloon when it satisfies these conditions. We show the overall average value, taken from each site in multiple calculated disordered lattices. We also identify the circle that circumscribes all three oxygen atoms that comprise the neck between Li1 and Li2 sites, again averaged over all sites of multiple simulations.

As can be seen in Figure 8, both the site size and the neck area increase with increased Ta doping. Since the lattice contracts, one might have imagined that the structure as a whole would contract, but our analysis shows that, evidently, the Ta ion pulls the neighboring O ions in more tightly than the Zr ion and that there is no compensating contraction of the Ta/ZrO₆ units toward one another. Alternatively, one could say that the LaO₈ distorted cubic units are somewhat rigid against the Ta–O bond contraction. Although the ND can only provide *average* bond lengths that include both Ta–O and Zr–O, this average can be examined, and a clear contraction as a function of Ta doping can be observed. For $x = 0.5/0.75$ in Li_{7-x}La₃Zr_{2-x}Ta_xO₁₂, we find average bond lengths for the TaO₆ and ZrO₆ octahedra of 2.07/2.02 Å. For the tetrahedral Li–O bonds, we find lengths of 1.91/1.92 Å, and for the octahedral Li–O bonds, we find the lengths between 1.84 and 2.30/1.83–2.33 Å. We find LaO₈ bond distances of 2.59/2.60 Å. All of these data support a picture of contracted TaO₆ octahedra along with rigid LaO₈ units that together contribute to an overall decrease in lattice parameter and simultaneous slight increase in the volume around both types of Li sites. The good correspondence between DFT and experiment in this regard gives us confidence in our Al-doping results, though actual quantitative comparison to experiment is impossible since there is no way to distinguish Li1 sites containing Al from Li1 sites that contain Li.

The structural situation for the Al-doped compounds is quite different from the Ta-doped compounds. Most available evidence points to Al having a strong site preference for the Li1 site,^{45–47} and we have therefore placed our Al dopants at this spot. It has also been suggested that beyond some level of Al incorporation shifts to Li2 sites or even to Al occupation of

non-Li sites with formation of secondary phases,⁴⁵ so we limit our Al content to within a range that this does not happen (less than 0.5 Al per formula unit). The inclusion of Al causes an overall expansion of the lattice as discussed previously. On a local scale, the site sizes change hardly at all as a function of Al doping (at least on average), but the neck size changes rather strongly. In fact, the neck size becomes a bimodal distribution (not shown), with a sharp peak around a very low value of ~ 1.7 and a much broader peak at a higher radius. By looking through our statistical data carefully, we track down the low peak to Li sites occupied by Al³⁺ ions. Al³⁺, therefore, causes a local contraction of the tetrahedral site it occupies but with an offsetting expansion of necks at other sites. Al³⁺ is thought to be immobile, so the local contraction simply reinforces (or perhaps causes) the immobility, and Li1 sites that are occupied by Al are effectively “blocking” to Li conduction, since it has been shown that Li must pass through the T_d site whether along the edge or through the center of the triangular neck.⁴⁸ In the data plotted in Figure 8 we have eliminated the highly contracted Al-occupied necks and averaged over only non-Al-occupied necks, which have a finite chance of Li passing through them. Since Al-doping has little effect on either site size but increases the average neck size, its inclusion might turn out to be beneficial for Li transport, despite the blocking effect. Even though some pathways would certainly become impassable, it could be the case that easier conduction through other adjacent, still available, pathways could compensate for the loss.

IV. SUMMARY

In summary, we combined ND, XRD, and Raman measurement in concert with density functional theory to carefully investigate the actual stoichiometry and structure of garnet type solid electrolyte Li₇La₃Zr₂O₁₂ with Ta and Al dopants. Our ND and XRD data provide consistent lattice constants and together reveal a slight overstoichiometry in Ta (as compared to the nominal value) and a moderate understoichiometry of Li. Comparing the calculated relative weight of Raman Ta (Zr)-peak with that from the Raman measurement, we also find that the actual Ta content in the samples is slightly higher than the nominal value, and we identify that source of the negative slope of Vegard’s law as a strong contraction of the TaO₆ octahedra in comparison to the ZrO₆ octahedra. The Ta and Li content-deviations do not charge balance each other, however. In combination with our observation that the measured lattice constant is larger than what is expected based on DFT calculations, we suggest that the charge balance is achieved via the presence of O vacancies. These simultaneously create/balance Li vacancies and enlarge the volume of the structure, bringing all observed and calculated quantities into agreement. Finally, we show the microscopic effects of Ta and Al doping on Li channel size in terms of Li1 and Li2 site sizes and the size of the neck that Li must pass through to travel between them. We show that while Ta enlarges all three quantities, Al leaves the site sizes unchanged while enlarging the neck. This provides the possibility of manipulating the Li ion conductivity by codoping with Al and Ta simultaneously to optimize both Li vacancy count and activation barrier.

■ ASSOCIATED CONTENT

Supporting Information

Tables T1–T3 showing the full ND refinement results; Figures S1 and S2 showing entropy change and ionic ordering variation

in calculated Raman spectra; Table T4 showing Vegard's law parameters cast as a function of vacancies, dopant concentration; Video V1 showing the lowest Raman active (breathing) mode. This material is available free of charge via the Internet at <http://pubs.acs.org>.

AUTHOR INFORMATION

Corresponding Author

*E-mail: michelle.johannes@nrl.navy.mil.

Notes

The authors declare no competing financial interest.

ACKNOWLEDGMENTS

We thankfully acknowledge computing resources from the NNIN/C at Cornell and Research Services at Boston College. The work at Cornell University was supported by NSF CBET Grant via contract numbers 1066406. Funding for M.D.J. and N.B. was provided by the Office of Naval Research through the Naval Research Laboratory's Basic Research Program. A portion of this research at ORNL's Spallation Neutron Source was sponsored by the Scientific User Facilities Division, Office of Basic Energy Sciences, U.S. Department of Energy. T.T. and J.S. would like to acknowledge support from the Revolutionary Materials for Solid State Energy Conversion, an Energy Frontier Research Center funded by the US Department of Energy, Office of Science, Office of Basic Energy Science under Award Number DE-SC001054. J.W. and J.L.A. would like to acknowledge support of the U.S. Army Research Laboratory (ARL).

REFERENCES

- (1) Orsini, F.; Du Pasquier, A.; Beaudoin, B.; Tarascon, J. M.; Trentin, M.; Langenhuisen, N.; De Beer, E.; Notten, P. J. *Power Sources* **1998**, *76*, 19–29.
- (2) Whittingham, M. S. *MRS. Bull.* **2008**, *33*, 419–420.
- (3) Kamaya, N.; Homma, K.; Yamakawa, Y.; Hirayama, M.; Kanno, R.; Yonemura, M.; Kamiyama, T.; Kato, Y.; Hama, S.; Kawamoto, K.; Mitsui, A. *Nat. Mater.* **2011**, *10*, 682–686.
- (4) Kotobuki, M.; Munakata, H.; Kanamura, K.; Sato, Y.; Yoshida, T. *J. Electrochem. Soc.* **2010**, *157*, A1076–A1079.
- (5) Tan, J. J.; Tiwari, A. *ECS Solid State Lett.* **2012**, *1*, Q57–Q60.
- (6) Murugan, R.; Thangadurai, V.; Weppner, W. *Angew. Chem., Int. Ed.* **2007**, *46*, 7778–7781.
- (7) Awaka, J.; Kijima, N.; Hayakawa, H.; Akimoto, J. *J. Solid State Chem.* **2009**, *182*, 2046–2052.
- (8) Geiger, C. A.; Alekseev, E.; Lazic, B.; Fisch, M.; Armbruster, T.; Langner, R.; Fechtelkord, M.; Kim, N.; Pettke, T.; Weppner, W. *Inorg. Chem.* **2011**, *50*, 1089–1097.
- (9) Allen, J. L.; Wolfenstine, J.; Rangasamy, E.; Sakamoto, J. *J. Power Sources* **2012**, *206*, 315–319.
- (10) Bernstein, N.; Johannes, M. D.; Hoang, K. *Phys. Rev. Lett.* **2012**, *109*, 205702.
- (11) Thompson, T.; Wolfenstine, J.; Allen, J. L.; Johannes, M.; Huq, A.; David, I. N.; Sakamoto, J. *J. Mater. Chem. A* **2014**, *2*, 13431–13436.
- (12) Blochl, P. E. *Phys. Rev. B* **1994**, *50*, 17953–17979.
- (13) Kresse, G.; Joubert, D. *Phys. Rev. B* **1999**, *59*, 1758–1775.
- (14) Perdew, J. P.; Burke, K.; Ernzerhof, M. *Phys. Rev. Lett.* **1996**, *77*, 3865–3868.
- (15) Perdew, J. P.; Burke, K.; Ernzerhof, M. *Phys. Rev. Lett.* **1997**, *78*, 1396–1396.
- (16) Kresse, G.; Furthmüller, J. *Phys. Rev. B* **1996**, *54*, 11169–11186.
- (17) Kresse, G.; Furthmüller, J. *Comput. Mater. Sci.* **1996**, *6*, 15–50.
- (18) Togo, A.; Oba, F.; Tanaka, I. *Phys. Rev. B* **2008**, *78*, 134106.
- (19) Larson, C. A.; Von Dreele, B. R. In *General Structure Analysis System (GSAS)*; Los Alamos National Laboratory: Los Alamos, NM, 2000.
- (20) Toby, B. H. *J. Appl. Crystallogr.* **2001**, *34*, 210–213.
- (21) Thompson, T.; Sharafi, A.; Johannes, M. D.; Huq, A.; Allen, J. L.; Wolfenstine, J.; Sakamoto, J. *Adv. Energy Mater.* **2015**, *5*, 1500096.
- (22) Hubaud, A. A.; Schroeder, D. J.; Key, B.; Ingram, B. J.; Dogan, F.; Vaughey, J. T. *J. Mater. Chem. A* **2013**, *1*, 8813–8818.
- (23) Rangasamy, E.; Wolfenstine, J.; Allen, J.; Sakamoto, J. *J. Power Sources* **2013**, *230*, 261–266.
- (24) Shimonishi, Y.; Toda, A.; Zhang, T.; Hirano, A.; Imanishi, N.; Yamamoto, O.; Takeda, Y. *Solid State Ionics* **2011**, *183*, 48–53.
- (25) Haas, P.; Tran, F.; Blaha, P. *Phys. Rev. B* **2009**, *79*, 085104.
- (26) Larraz, G.; Orera, A.; Sanjuan, M. L. *J. Mater. Chem. A* **2013**, *1*, 11419–11428.
- (27) Buschmann, H.; Berendts, S.; Mogwitz, B.; Janek, J. *J. Power Sources* **2012**, *206*, 236–244.
- (28) Logeat, A.; Koehler, T.; Eisele, U.; Stiasny, B.; Harzer, A.; Tovar, M.; Senyshyn, A.; Ehrenberg, H.; Kozinsky, B. *Solid State Ionics* **2012**, *206*, 33–38.
- (29) Thangadurai, V.; Adams, S.; Weppner, W. *Chem. Mater.* **2004**, *16*, 2998–3006.
- (30) Wang, Y. X.; Lai, W. *Electrochem. Solid-State Lett.* **2012**, *15*, A68–A71.
- (31) Zeier, W. G.; Zhou, S.; Lopez-Bermudez, B.; Page, K.; Melot, B. C. *ACS Appl. Mater. Interfaces* **2014**, *6*, 10900–10907.
- (32) Ramakumar, S.; Janani, N.; Murugan, R. *Dalton Trans.* **2015**, *44*, 539–552.
- (33) Ramakumar, S.; Satyanarayana, L.; Manorama, S. V.; Murugan, R. *Phys. Chem. Chem. Phys.* **2013**, *15*, 11327–11338.
- (34) Kim, Y. M.; He, J.; Biegalski, M. D.; Ambaye, H.; Lauter, V.; Christen, H. M.; Pantelides, S. T.; Pennycook, S. J.; Kalinin, S. V.; Borisevich, A. Y. *Nat. Mater.* **2012**, *11*, 888–894.
- (35) Murat, A.; Medvedeva, J. E. *Phys. Rev. B* **2012**, *86*, 085123.
- (36) Seo, S. S. A.; Marton, Z.; Choi, W. S.; Hassink, G. W. J.; Blank, D. H. A.; Hwang, H. Y.; Noh, T. W.; Egami, T.; Lee, H. N. *Appl. Phys. Lett.* **2009**, *95*, 082107.
- (37) Shah, L. R.; Ali, B.; Zhu, H.; Wang, W. G.; Song, Y. Q.; Zhang, H. W.; Shah, S. I.; Xiao, J. Q. *J. Phys.: Condens. Matter* **2009**, *21*, 486004.
- (38) Wang, X. J.; Vlasenko, L. S.; Pearton, S. J.; Chen, W. M.; Buyanova, I. A. *J. Phys. D Appl. Phys.* **2009**, *42*, 175411.
- (39) Wang, Z. L.; Yin, J. S.; Jiang, Y. D. *Micron* **2000**, *31*, 571–580.
- (40) Nymann, M.; Alam, T. M.; McIntyre, S. K.; Bleier, G. C.; Ingersoll, D. *Chem. Mater.* **2010**, *22*, 5401–5410.
- (41) Wolfenstine, J.; Allen, J. L.; Read, J.; Sakamoto, J. *J. Mater. Sci.* **2013**, *48*, 5846–5851.
- (42) Xie, H.; Alonso, J. A.; Li, Y. T.; Fernandez-Diaz, M. T.; Goodenough, J. B. *Chem. Mater.* **2011**, *23*, 3587–3589.
- (43) Adachi, G. Y.; Imanaka, N.; Aono, H. *Adv. Mater.* **1996**, *8*, 127–&.
- (44) Miara, L. J.; Ong, S. P.; Mo, Y. F.; Richards, W. D.; Park, Y.; Lee, J. M.; Lee, H. S.; Ceder, G. *Chem. Mater.* **2013**, *25*, 3048–3055.
- (45) Rettenwander, D.; Blaha, P.; Laskowski, R.; Schwarz, K.; Bottke, P.; Wilkening, M.; Geiger, C. A.; Amthauer, G. *Chem. Mater.* **2014**, *26*, 2617–2623.
- (46) Wang, D. W.; Zhong, G. M.; Dolotko, O.; Li, Y. X.; McDonald, M. J.; Mi, J. X.; Fu, R. Q.; Yang, Y. J. *J. Mater. Chem. A* **2014**, *2*, 20271–20279.
- (47) Buschmann, H.; Dolle, J.; Berendts, S.; Kuhn, A.; Bottke, P.; Wilkening, M.; Heitjans, P.; Senyshyn, A.; Ehrenberg, H.; Lotnyk, A.; Duppel, V.; Kienle, L.; Janek, J. *Phys. Chem. Chem. Phys.* **2011**, *13*, 21658–21659.
- (48) Wang, Y.; Klenk, M.; Page, K.; Lai, W. *Chem. Mater.* **2014**, *26*, 5613–5624.